Contents lists available at ScienceDirect

Biosensors and Bioelectronics

journal homepage: www.elsevier.com/locate/bios

Modelling a dynamic magneto-agglutination bioassay

Robert Hughes [a,*], Aaron Fishman [b], Kathryn Lamb-Riddell [c], Valentina Sleigh Muñoz [b], Alan Champneys [b], Janice Kiely [c], Richard Luxton [c]

[a] Department of Mechanical Engineering, University of Bristol, Bristol, BS8 1TB, UK
[b] Department of Engineering Mathematics, University of Bristol, Bristol, BS8 1TW, UK
[c] Institute of Bio-Sensing Technology, University of West of England, Bristol, BS34 8QZ, UK

A B S T R A C T

The process of developing an end-to-end model of a magneto-immunoassay is described, simulating the agglutination effect due to the specific binding of bacteria to paramagnetic particles. After establishing the properties of the dose-specific agglutination through direct imaging, a microfluidic assay was used to demonstrate changes in the magnetophoretic transport dynamics of agglutinated clusters via transient inductive magentometer measurements. End-to-end mathematical modelling is used to establish the physical processes underlying the assay. First, a modified form of Becker–Döring nucleation kinetic equations is used to establish a relationship between analyte dose and average cluster size. Next, Stokes flow equations are used to establish a relationship between cluster size and speed of motion within the fluid chamber. This predicts a cluster-size dynamic profile of concentration of PMPs versus time when the magnetic field is switched between the two actuated magnets. Finally, inductive modelling is carried out to predict the response of the magnetometer circuit in response to the dynamics of magnetic clusters. The predictions of this model are shown to agree well with the results of experiments, and to predict the shape of the dose-response curve.

1. Introduction

Recent global health crises have emphasised the importance of rapid testing procedures for the detection of disease Luppa et al. (2011). Widespread point-of-care (POC) testing could enable almost real-time tracking of disease, which could allow epidemics to be contained (He et al., 2020) and enable more targeted prescription of antibiotics (Bean et al., 2008; O'Neill, 2014). More generally, rapid POC diagnosis is a key ingredient for the emerging paradigm of personalised medicine.

Most POC diagnostic assays seek to identify specific biological or chemical markers of infection, such as bacteria or viral antigens. Specifically, immunoassays use antigen-antibody binding to test for concentrations of a certain targets e.g. Hu et al. (2007). Examples include the common pregnancy test using a gonoadotrphin marker within urine, and the glucometer that measures a diabetic's blood glucose level (Hönes, Müller and Surridge, 2008). The key to success is to have a rapid reporter mechanism; electrochemical for the glucometer, and colour producing enzymes for the pregnancy test.

The requirements for any POC diagnostic device is that it should be ASSURED; that is *affordable, sensitive, specific, user-friendly, rapid and robust, equipment-free*, and *deliverable* to end users (Naseri et al., 2021; Sista et al., 2008). Moreover the report mechanism should be rapid and have a proportional response, even at low dose levels.

Diagnostic quantification and sensing techniques include electro-chemical, electrostatic, fluorescence, colorimetric, and magnetic bio-sensors to name only a few (e.g. see Tepeli and Ülkü, 2018; Foudeh et al., 2012; Wang et al., 2021). There is also value in using combined approaches, for example; Ahmadivand et al. (2017) show that magneto-optical systems can have significant advantages over purely optical approaches, and Gopal et al., 2013 enhance the power of a mass-spectroscopy biosensor using magnetoparticles.

Many developments employ technologies from the growing fields of fluidic and electronic miniaturisation using microfluidics, nano-materials and micro electro-mechanical systems (MEMS) (Islam and Saye, 2012; Manz, Neuzil, O'Connor and Simone, 2020; Wang et al., 2020; Sachdeva et al., 2021).

One of the key difficulties in designing new rapid POC immunoassays is the lack of quantitative understanding of the underlying physics, so that device development requires a trial and error approach. A notable exception is the work of Wua and Voldman (2020), who develop and analyze a semi-homogeneous bead-based electronic enzyme-linked immunosorbent assay and show how it can provide design guidance for choice of various assay parameters.

The aim of the current paper is to develop a similar multiphysics model for a novel kind of immunoassay that uses micro-fluidic magnetic bead actuation, combined with the principle of agglutination. In such an

assay, the average cluster size is a marker for the dose response, and our modelling of the underlying viscous fluid dynamics enables us to establish that the particle dynamics are cluster-size dependent, which in turn can be detected by a magnetometer.

The paper is outlined as follows: Section 2 outlines the biochemistry of the binding of target molecule to the PMPs. Section 3 then explains the experimental protocol of the microfulidic assay and 4 presents experimental data demonstrating a reliable dose response. Section 5 then undertakes end-to-end modelling of the various dominant physical processes taking place, in order to understand the theoretical basis for the experimentally observed dose response. Finally, Section 6 draws conclusions and suggests avenues for future work.

2. Underlying biochemistry

This work is part of a wider study that seeks to build and optimise an immunoassay to analyze urine samples to screen for the main bacteria that can cause a urinary tract infection, the most common of which is *Escherichia coli* (*E. coli*). This study builds on previous work by the present authors and their collaborators (see Roberts et al., 2017; Sharif et al., 2013 and references therein) who have developed assays based on paramagnetic particles (PMPs) coated with target-specific antibodies (Tsouris and Scott, 1995; Barnett and Wraith, 2014). A magnetometer is used to measure the temporal change in magnetic field strength induced by the PMPs as they are pulled away from the sensor by permanent magnets. Magneto-immunoassays are also particularly amenable for miniaturisation using microfluidics (Delaney and Suh-Lailam, 2018).

2.1. Agglutination

Agglutination is the process by which particles bind together as a result of molecules on the surface of the particle interacting with other particles, often associated with an antibody on the surface of the cell (see Stavitsky, 1998 and references therein).

The ability of multivalent antibodies to cross-link multivalent antigens, or targets, has been used to quantify specific antigens in biological fluids since the 1930's. Insoluble precipitates are formed when antibody molecules form a network of multiply cross-linked antigens. As the quantity of antigen increases, relative to antibody, the amount of insoluble precipitate increases to reach a maximum. At this point there is an optimum ratio of antibody to antigen allowing a maximum number of cross-linking interactions to occur. This is known as the *equivalence zone* and if the amount of antigen increases even further the system is known to be in *antigen excess*. When the state of antigen excess exists, less precipitate is formed due to excess antigen *smothering* the antibody, thus preventing it from cross-linking multiple antigens and thereby reducing the amount of insoluble precipitate being formed. For a fixed amount of antibody to which an increasing amount of antigen is added the quantity of insoluble precipitate formed follows a bell-shaped curve known as the Heidelberger-Kendall or just Heidelberger curve (Heidelberger and Kendall, 1934; Heidelberger, 1939), sometimes referred to as the 'hook effect' (see also Roberts et al., 2017; Sharif et al., 2013 for a mathematical prediction of this curve shape).

Antibody coated latex or magnetic particles can enhance the detectability of agglutination and extend the range of the positive dose response before antigen excess prevents cross-linking of particles. There are many examples of agglutination of particles being used as a method to detect and quantify molecules and bacteria in the investigation of disease. For example, Wu et al. (2020), used coated gelatin particles to measure antibodies to Mycoplasma pneumoniae. Also, Qu et al., 2021, used antibody coated paramagnetic particles to measure the C-reactive protein by monitoring agglutination of the particles using light-scattering on a fluidic chip.

2.2. Paramagnetic particles

The magnetic immunoassay described in this paper uses PMPs and an inductive magnetometer to measure the concentration of bacteria. The procedure varies in a number of ways to the assay studied by Roberts et al. (2017), the most obvious of these being that it is not a sandwich assay. The assay in Roberts et al. (2017), also involves target antigens that are small compared to the PMPs, whereas here the target bacteria, *E. coli*, has a similar length to the PMPs (approximately 1–2.8 μm). Their similar sizes mean that there are far fewer bound bacteria to each PMP than there were bound target antigens to each PMP in the sandwich assay. Fig. 1.a and b show the relative sizes of the PMPs and *E. coli* bacteria under both an atomic force microscope (AFM) and a scanning electron microscope (SEM) respectively. Note from these images that the PMPs are spherical and the *E. coli* bacteria have a rod-like shape. The geometry and sizes of the particles and the bacteria do not allow all the antigens on the surface of a bacterium to bind to all the antibodies on the surfaces of the surrounding PMPs, therefore the number of actual binding sites is lower than the number of potential binding sites. This observation will be used to justify various modelling assumptions used in Section 5. However, even with a small number of binding sites, the images show how the bacteria and PMPs can agglutinate through antigen-antibody bonding to form relatively large clumps of particles and bacteria.

2.3. Target bacteria

Escherichia coli (*E. coli*), a gram-negative bacillus measuring approximately 1 μm long by 0.35 μm wide, is a common inhabitant of human and animal lower intestinal tracts. It is one of the most common laboratory model microorganisms, widely used in bacterial physiology, molecular biology and biotechnology. Most *E. coli* strains rarely cause disease except when normal host immunity has been compromised. Nevertheless some strains express additional virulence factors and may cause significant disease even in healthy humans, including urinary tract infection, diarrhoea, meningitis and sepsis (Kaper et al., 2004). Also, Shiga toxin producing *E. coli* (STEC) can cause outbreaks of food-borne disease, and can cause life-threatening infection, while *E. coli* serotype O55 is a common cause of infant diarrhoea both in developing countries (Stenutz et al., 2006) and the developed world (McFarland et al., 2017). More generally, the presence of *E. coli* in the environment is commonly used as an indicator of recent faecal pollution (Jang et al., 2017). The present study uses *E. coli* serotype 55.

2.4. Preparation of PMPs

Protein G Dynabead^{TM} 2.8 μm paramagnetic particles (Sigma, UK) were coated with Abcam ab137967 rabbit polyclonal anti-Escherichia coli antibodies using the following method: Particles were prepared by removing the storage buffer using a magnetic rack and resuspending 50 μl beads with 200 μl 5 μg/ml antibody in 0.01M pH7.2 Phosphate Buffered Saline (PBS) with 0.02% Tween 20. The particles were incubated with rotation for 10 min at room temperature, then returned to the magnetic rack and the supernatant removed. The antibody-bead complex PMPs were then re-suspended in 200 μl PBS with Tween 20.

The concentration of stock Ab-PMPs were determined by diluting a well-mixed aliquot in PBS, and gently pipetting 10 μl of the suspension into a KOVA FastRead102 (VWR, UK) cell counting chamber. The PMPs were allowed to settle for 5 min and imaged using an Olympus CKX53 inverted microscope and CellSense imaging software. The mean of 32 replicates was used to calculate the stock concentration of antibody-coated PMPs. The PMPs were then diluted when required in PBS to give a final concentration of 10^7 PMPs/ml.
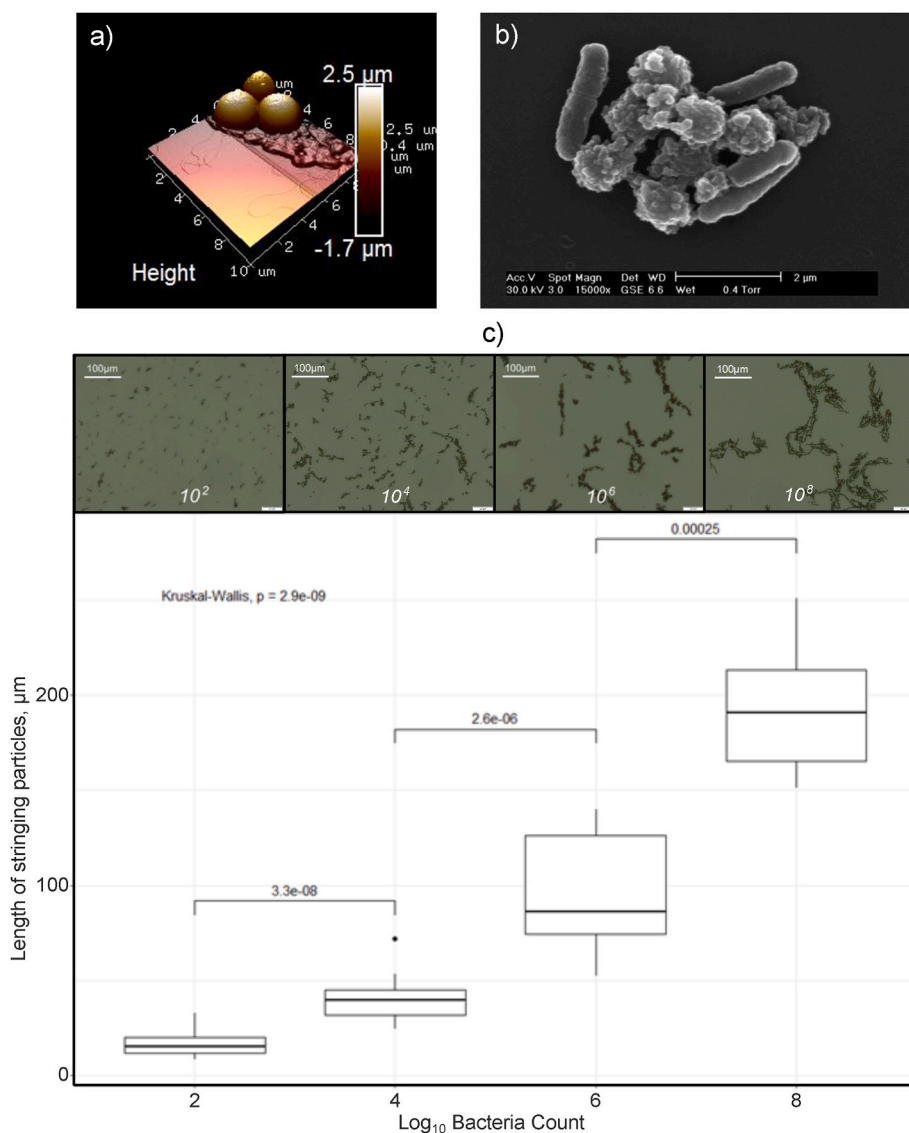
Fig. 1. Agglutination dose response - *a*) An atomic force microscopy (AFM) height map of PMPs bound to E.coil. *b*) A scanning electron microscope (SEM) image of PMP's bound to E. Coli. The PMP's are the spherical shapes and the *E. coli* bacteria are the rod-like shapes. *c*) Optical microscope images at different bacterial concentrations between $0 - 10^8$ cfu/ml, and *b*) a boxplot of the measured length of stringing particles at different bacterial concentrations. Pairwise comparisons are based on a Wilcoxon test.

2.5. Bacteria & culture conditions

*Escherichia coli*O55 was grown for 18 h in 10 ml NB broth (Oxoid, UK) in a static incubator at 37 °C. The overnight culture was then diluted 10-fold in 0.01M pH7.2 Phosphate Buffered Saline (PBS) for optical and AFM imaging. The colony forming units (cfu/ml) of bacterial samples was determined by surface spreading the diluted samples on Nutrient Agar (Oxoid, UK) and counting visible bacterial colonies after 18–24h incubation at 37 °C.

2.6. Sample agglutination & optical imaging

A 100 μl aliquot of each diluted *E.coli* suspension (or a negative control of PMPs only) was added to 100 μl PMP suspension and incubated at 25 °C for 10 min to allow agglutination to occur. For optical imaging, 10 μl of the incubated suspension was gently pipetted into a KOVA FastRead102 (VWR, UK) cell counting chamber and the PMPs allowed to settle for 5 min. Images of the samples were then captured using an Olympus CKX53 inverted microscope and CellSense imaging software (Olympus, UK).

Fig. 1.c shows optical images captured for increasing numbers of bacteria mixed with the 10^6 PMPs. Note how the images show how agglutination form into string-like chains of alternating PMP and

bacteria and that the typical chain length increases with dose. To quantify this effect, the software of ImageJ was used to record typical chain lengths in each image, in units of pixel length, which is then converted to microns. Fig. 1.c shows a box-plot of the length of stringing particles found with differing numbers of bacteria, with a fixed number of PMPs. The results show a highly significant difference in the chain length particles with numbers of bacteria, over six orders of magnitude.

2.7. Microscopy

More details of the structures formed through chain-like agglutination were obtained using SEM and AFM imaging (see Fig. 1.a & b. for example images). It was found that the structures formed at higher doses remain chain-like but can also 'wrap up' to form more tightly clustered superstructures.

For the AFM imaging, mica discs were prepared by cleaving using adhesive tape and then coating with 5μ l 0.01% poly-l-lysine (Sigma, UK) as an immobilisation agent. 10 μl of the PMP and bacteria suspension was gently pipetted onto the coated mica. The samples were then incubated at 25 °C for 15 min and then washed with PBS. Samples were fixed with 2.5% glutaraldehyde for 15 min before being washed 10 times with sterile filtered water (Sigma, UK), and then dried in air at 25 °C for 30 min before scanning with an Innova (Bruker, UK) AFM imaging. The

images were captured in tapping mode using aluminium coated silicon probes at scan speeds between 0.3 and 1.0 Hz and a resolution of 512 by 512 pixels. Images were processed using Nanoscope (Bruker, UK) with plane fitting where required.

3. Agglutination assay design and operation

The assay we seek to model is shown schematically in Fig. 2.b. It uses PMPs coated with an antibody that binds to specific proteins on the bacteria cell surface thereby causing an agglutination reaction. The reporting method we use exploits the variation in drag forces on clusters of different size when being dragged through a viscous fluid by a magnetic field. This variation in drag force then leads to a change in the dynamics of the particles, which can be detected by an inductive magnetometer. The process of taking the measurement can be broken down into a number of steps.

First, a sample, containing an undetermined concentration of bacteria is injected, at a uniform rate, into a 3D printed microfluidic testing chamber (4×5 *mm* cross-section) containing the PMPs. This so-called *mixing stage* takes around 90 s (see Fig. 2.d 90–180s).

The second stage of the assay relies on measuring changes in the magnetometer coil inductance due to the dynamic motion of PMPs being pulled away from the magnetometer by actuated permanent magnets. The two magnets and the geometry of the chamber are designed to keep the PMPs inside the chamber as magnetic manipulation occurs. When one of the magnets is first moved into the 'on' position (see Fig. 2.b), the PMPs, and the bacteria that have attached to them, are attracted towards that magnet. Fig. 2.c contains images taken from this stage of the

immunoassay. The individual frames show the movement of clumps of PMPs towards the top magnet which is in the 'on' position (Fig. 2.c.ii). Throughout the experiment, top and bottom magnets are alternated into the 'on' positions, undergoing repeat cycles (or Reps) of the process. The clumps of particles and bacteria are attracted accordingly, being alternately pulled between the top and bottom of the chamber. The dynamic change in local magnetic field strength around the magnetometer is measured continuously (Fig. 2d). In principle the more clustering there is then the more PMPs there are in close proximity to each other, which should be detectable in the transients of how the magnetometer responds to a switch between a magnet being 'on' or 'off'.

3.1. Inductive magnetometer

In order to detect the minor variations in the local magnetic field strength due to the agglutination of PMP and bacteria, a frequency-locked loop magnetometer circuit developed by Wraith Innovation Solutions Engineer (UK) was used. Here, a very high frequency (VHF) variable voltage controlled oscillator (VCO) is used to create a stable electrical measurement of a 3.5 mm diameter planar spiral PCB coil at its resonant frequency of 85 MHz (Barnett and Wraith, 2014). The measurement system, controlled for temperature fluctuations, measures shifts in the resonant frequency, f_0, of the magnetometer coil caused by changes to its local magnetic environment. PMP particles increase the magnetic permeability of local area thereby increasing the inductance, L, of the coil causing a resonant frequency shift as defined by the formula,
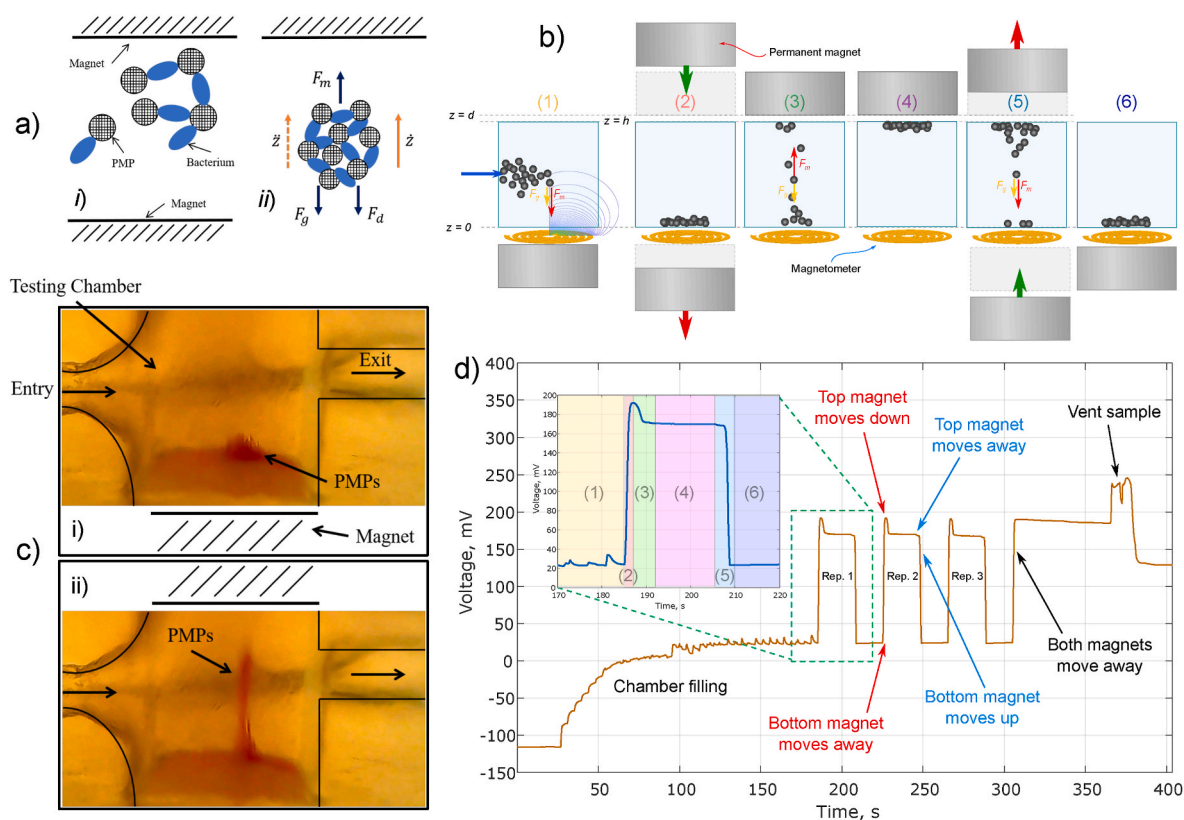

Fig. 2. Magneto-agglutination assay principles - *a.i*) A schematic diagram of the magnetic immunoassay. *a.ii*) A free body diagram showing the forces acting on a cluster of size *n* in the presence of a magnetic field. The forces acting on the cluster are the magnetic force F_m, the drag force F_d and the gravitational force F_g. Velocity is represented by $\dot{z}$ and acceleration by $\ddot{z}$ *b*) Schematic diagram of magneto-agglutination assay process for a single repeat (Rep.) of the measurement showing the 6 phases. *c*) Side-on video images of the testing chamber (4 mm × 5 mm) taken during the experiment when the top magnet has just been turned on *i*). The PMPs (in red) can be seen beginning to be moving upwards while *ii*) shows the same sample a few seconds later showing a clear column of PMPs moving towards the magnet above. Images provided by the Health Tech Hub, Kiely and Luxton (2022), annotated by the authors. *d*) an example magnetometer response trace, showing the phases of the measurement and the 3 repeats (Rep.1-3) per sample.

$$f_0 = \frac{1}{2\pi\sqrt{LC}}, \tag{1}$$

where C is the capacitance of the system (Hughes and Dixon, 2018). For a system with high resonant frequency and small inductance, a small variation in L will result in a larger change in f_0. A resonant frequency limit of 85 MHz was used to avoid electromagnetic interference from FM radio broadcasts (87.5–108 MHz). Further details of the magnetometer system can be found in Barnett and Wraith (2014). The measurement is similar to that use by Pai et al. (2014), who examined the resonant frequency shifting of a 1 GHz inductive oscillator during "magnetic freezing" (fixing of magnetic microbeads) as a fast and low-cost biological assay.

3.2. The measurement protocol

An example magnetometer response plot is presented in Fig. 2.d, showing the full magneto-agglutination assay, highlighting key features of the process and magnet positions.

After filling the assay chamber with buffer, the assay follows the process summarised below, and highlighted in Fig. 2.b & d:

1. PMP-bacteria sample mixture is pumped into the chamber where a permanent magnet attracts the PMP to the bottom of the chamber (1).
2. The bottom permanent magnet is withdrawn and the top magnet is introduced above the chamber (2).
3. The PMPs are attracted to the top magnet against the force of gravity (3).
4. PMPs accumulate at the top of the chamber (4).
5. The top magnet is withdrawn, simultaneously with the bottom magnet being re-introduced causing the PMP's to fall back to the bottom of the chamber under the combined magnetic and gravitational force (5).
6. Having come to rest (6), the process is repeated a total of 3 times before the magnets are withdrawn and the sample is vented from the chamber.

Analysis of the magneto-agglutination assay time-trace is performed in Matlab, by isolating the repeated particle manipulation sections of the trace. A key property of the signal that was found to be most sensitive to the number of PMPs and concentration of the target was the dynamics of the transient process between stages (2) and (3) depicted in Fig. 2.b & d.
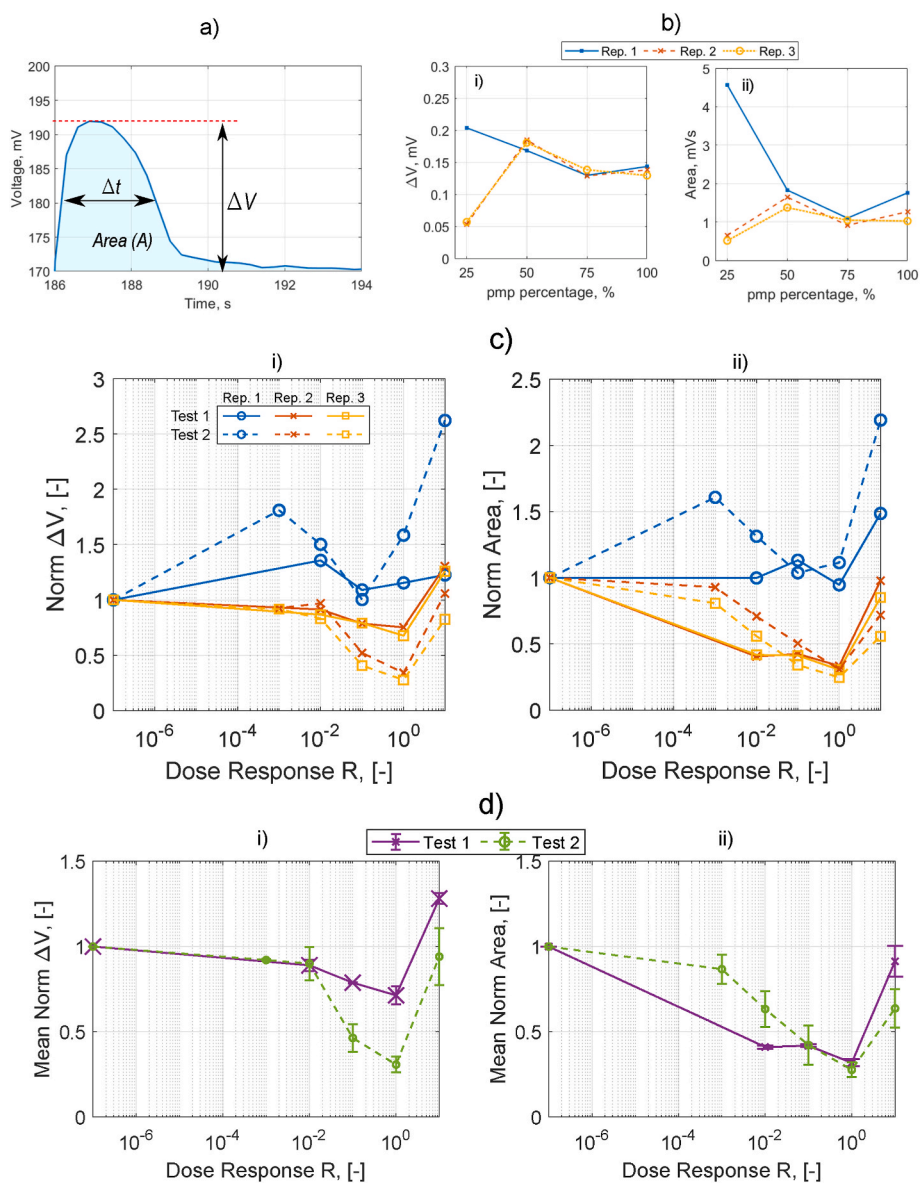

Fig. 3. Experimental magneto-agglutination tests - *a*) Example transient inductive decay response and measurement metrics. *b*) PMP percentage study: Experimental inductive response metrics as a function of PMP percentage used for each magnet motion cycle repeat (Rep.), showing i) normalised peak voltage, ΔV, and ii) area under the curve, A. 100% PMP concentration is equivalent to 10^7 *pmp/ml*. Bacteria concentration study: *c*) Experimental normalised magnetometer time-response metrics for each repeat as a function of bacteria dose response ratio, R, for 2 assay tests showing; i) ΔV, and ii) A, and (*d*) shows the mean of the normalised responses from Rep. 2 & 3 in each assay time-trace (Test 1 & 2) for metrics i) ΔV, and ii) A.

To facilitate comparison between repeats and different concentrations, these transient decay signals were normalised to the plateaued amplitude and critical metrics of the time-traces analysed; specifically the area under the curve, *A,* and the peak voltage, ΔV, see Fig. 3.a. Also highlighted is the peak width, Δt, which is equivalent to *A* by multiplication with ΔV. These quantities are the key outputs of the assay.

4. Experimental results

The process outlined in Section 2.6 was conducted in the same sample chamber for a series of *E. coli* bacterial concentrations mixed with a solution of PMP's with concentration $\approx 10^7$ pmp/ml. Fig. 3 shows the resulting dose response curves for two tests using the different time-trace metrics. The results are shown as a function of the ratio, *R,* between bacteria and PMPs in solution. The output is normalised to the corresponding response for zero dose (a solution containing only buffer and PMPs without bacteria).

To test the robustness of the assay, a control study was conducted to test whether the response is dominated by the number of PMPs in the sample rather than bacterially-induced agglutination. To test this possibility, we carried out the magneto-assay on a series of PMP percentage dilutions to create solutions containing buffer and a varying concentrations of PMPs. These concentrations were subjected to the same magneto-agglutination assay process shown in Fig. 2.b.

The results are shown in Fig. 3.b, which highlights an effect where higher concentrations of PMPs increase the speed of extraction, thereby reducing *A*. This is most likely a result of cooperative magnetophoresis (Faraudo et al., 2016) where PMPs self-assemble forming larger, more magnetically receptive, clusters inside a magnetic field. Nevertheless this effect seems to saturate at PMP concentrations about 50% of the 'full concentration' of 10^7 pmp/ml, and the control test demonstrates that in the absence of bacteria, there is little difference between Rep. 1–3.

Fig. 3.c shows the normalised inductive response curve metrics for each of three repeats (Rep.'s) in the time response curve (see Fig. 2.d) for each bacterial concentration dose. Each figure compares the results from two tests, where each measurement is carried out for a new batch of diluted bacteria concentrations. Test 1 analysed four bacterial solution concentrations from 10^5 to 10^8 bacteria per ml ($R = 10^{-2} - 10^1$), while Test 2 analysed five concentrations from 10^4 to 10^8 bacteria per ml ($R = 10^{-3} - 10^1$). The two panels of Fig. 3.c show the normalised responses for the peak voltage, ΔV, and area under curve, *A*.

It is clear from Fig. 3.c-d that the selected inductive response metrics each exhibit a dip in magnitude between $10^{-1} - 10^0$ in the dose response curve. Moreover, there is a gradual decline in each metric as the dose increases towards full saturation ($R = 1$), with a rapid increase beyond saturation ($R = 10$). Due to the variance observed between the first repeat (Rep. 1) and subsequent repeats (Rep. 2–3) in each assay test (see Fig. 3c), it was concluded that the dynamic magnetophoretic forces initiate some additional interactions, most likely greater magnetic attraction between PMPs leading to further agglutination. It was therefore concluded that only the stabilised Reps 2 & 3 would be used to assess the dose response from the data. The means of the normalised metrics for both assay tests are therefore shown in Fig. 3.d along with the errorbars between Reps 2–3. This demonstrates a clear dose response, with high repeatability between repeats 2–3 of the biosensor.

Note that the inverted bell, or hook-shaped dose response seen in Fig. 3.d is a classic example of a Heildelberger curve (Heidelberger and Kendall, 1934; Heidelberger, 1939). A simple rationale for this shape of the dose response curve in the assay can be understood in terms of the time it takes for the transient signal to decay. The more agglutination that occurs between PMPs and bacteria, the larger the size and effective magnetic susceptibility of the resulting clumps under the magnetic force. This larger size will increase the inertia, gravitational force and resistance to fluid flow, however, the increased magnetic susceptibility of a closely-packed PMP cluster will increase the force acting upon it reducing *A*. Thus, for a fixed number of PMPs, and all other conditions

the same, we would expect that a decrease in *A* correlates with an increase in target concentration, until the PMPs are as densely packed as they can be (i.e. all are used). At that point, any addition of bacteria to the clumps serves to increase the inertia and resistance to flow without increasing the magnetic susceptibility, thereby reducing the rate of movement — increasing *A*.

However, the effect is clearly subtle and its quantification requires detailed mathematical modelling to understand how each step of the assay protocol depends on the concentration of target. The derivation of such a model is reported in Section 5 below and is the main focus and novelty of this paper.

5. End-to-end mathematical modelling

In order to understand the relationship between target dose and magnetometer measurement, and to form a theoretical basis to the proposed metric for dose response, we have built a full model of the agglutination magneto-assay process. The model comprises a number of separate components; the process of agglutination clustering, the distribution of magnetic forces within the chamber, the dynamics of magnetophoretic particle clusters under this force, and the inductive magnetometer response to clusters of particles at different positions within the chamber. Each step in this end-to-end modelling process is outlined in each of the following subsections. The technical details and simplifying assumptions are provided in Supplementary Materials.

5.1. Kinetics of agglutination

The kinetics of agglutination is a complex process that involves the formation of clusters involving cross-links between PMPs and bacteria. Looking at the images in Fig. 1.c, we see that the clusters are string-like, characterised mostly by long chains of cross-linked PMPS, which occasionally reconnect. The main difference between the four images in Fig. 1.c, representing increased bacterial concentration, seems to be the average length of each of these chains. Specifically: at zero target concentration, the chain length seems to be about $\mathcal{O}(2^1)$ PMPs, at bacterial concentration of 10^2, the number of PMPs in a chain is $\mathcal{O}(2^3)$, at concentration 10^4 the typical chain length is $\mathcal{O}(2^5)$, at concentration 10^6 chain length is $\mathcal{O}(2^7)$, and at concentration 10^8, $\mathcal{O}(2^9)$. This suggests a relationship for fixed number of PMPs of,

$$\text{chain length} \propto \ln(\text{bacterial dose}). \qquad (2)$$

In order to justify such a relationship, we have undertaken a model of cluster formation, using so-called Becker-Döring theory (see Becker and Döring, 1935; Ball et al., 1986; Wattis and King, 1998 and references therein). More details of the model development can be found in the Supplementary Material, Section 5.1, and Sleigh Muñoz (2020) (available from the authors upon request).

The basic principle is that long chains of successive bacteria and PMPs form via the law of mass action applied to chains of smaller length. The simple Becker-Döring paradigm was extended in two different ways: First, we include two different species, namely bacteria and PMPs. Second, we allow the possibility that chains of length $n_1 + n_2$ can form from binding with chains of length n_1 and n_2 for $n_{1,2} > 1$. To model the effect that such reactions are likely to occur with lower affinity than those that involve a single PMP or bacterium joining a chain, a dimensionless parameter κ is introduced so that $\kappa = 0$ means all reactions occur with equal probability where as $\kappa > 0$ means that longer chains bind with less probability than shorter ones. Nevertheless the results were not found to depend strongly on the value of κ.

While the principle is straightforward, the resulting equations are somewhat cumbersome, due to the combinatorial increase in different possible reaction steps with the maximum size *N* of clusters involved. The details are given in the Supplementary Material 5.1. The key input to the model is a single dimensionless parameter, β, which is the initial

ratio of bacteria to PMPs. That is, β directly parameterise the dose of the target molecule in the sample.

It was found to be unrealistic to run for higher $N \approx 70$ due to the combinatorial explosion of complexity. Nevertheless clear trends were found and the shape of distribution of cluster sizes was found to be mostly a function of dose β, rather than N or κ. Typical distributions are given in Fig. 4.c.

5.2. Magnetophoresis

Magnetophoresis is the process of describing the magnetic force experienced by a magnetically susceptible body. Our aim is to describe the magnetic force acting on a cluster of PMPs, but first we need to calculate the magnetic force, F_p^m, acting on a single PMP, with susceptibility χ_p, for a given magnetic flux-density, $\mathbf{B_m}$, acting at a given point.

The magnetic flux-density of the permanent magnets used was experimentally measured along its z-axis (the vertical co-ordinate direction which separates the 'top' and 'bottom' of the chamber, which is also aligned with gravity) using a Hall-effect sensor.

The results are shown in Fig. 4.a and compared to the simulated magnetic flux-density calculated using the Biot-Savart law for a current loop (see, e.g. Griffiths, 2008). For a permanent magnet of height h and radius a, with its face located a distance d from the bottom of the assay chamber (at $z = 0$), the law can be expressed in the form,

$$\mathbf{B}_m = \frac{B_0 a^3}{\left[(z - d_0)^2 + a^2\right]^{3/2}} \; \widehat{\mathbf{z}}, \tag{3}$$

where a is the radius of the magnet/current-loop and B_0 is the magnetic flux density in the plane of the current loop (at $z = d_0 = d + h/2$ mm). B_0 is calculated from the measured value at the surface of the permanent magnet ($z = d$ mm).

For a given $\mathbf{B_m}$, the force F_p^m on a individual PMP can be estimated
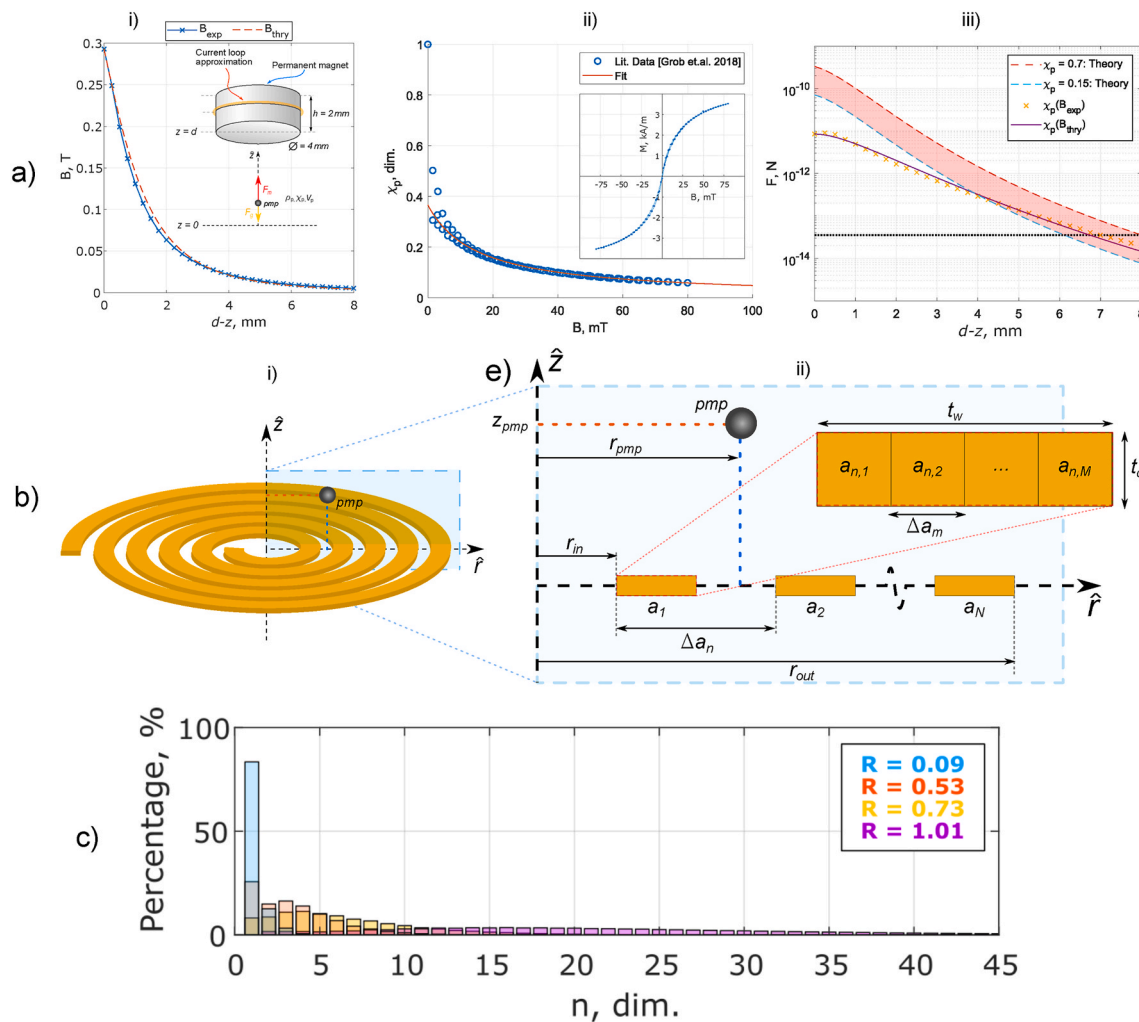

Fig. 4. Modelling - a) Magnetophoretic force on a PMP showing: i) the magnetic flux-density, $\mathbf{B}_m$, of the permanent magnetic used to perform magnetophoresis on PMP's showing experimental measurements compared to a Biot-Savart current loop model, with (inset) the geometry of the magnetic field theoretical current loop model relative to the permanent magnet position. ii) The experimentally measured magnetic susceptibility of 2.8 μm Dynabeads® as a function of the magnetic flux density, from Grob et al. (2018), along with a line of best (red curve). iii) The magnetic force, F_m, acting on a PMP as a function of relative position to the face of the permanent magnet for different constant magnetic susceptibilities compared to the magnetic flux density dependant susceptibility from (ii). b) Schematic diagram of the inductive sensor model showing i) the spiral coil geometry and ii) the finite filament approximation of the coil turns. Diagrams created and annotated by the author, after Gal-Katziri and Hajimiri (2019). c) shows the percentage of each cluster size formed after a settling time for different PMP-bacteria ratios, β (called R in the legend), calculated for $N = 70$.

using standard principles (Shevkoplyas et al., 2007):

$$\mathbf{F}_p^m = \frac{V_p \Delta\chi_p}{\mu_0}\left(\mathbf{B_m} \cdot \frac{\partial}{\partial z}\right)\mathbf{B_m}$$

$$= 3\frac{V_p B_0^{\ 2}}{\mu_0}\frac{a^6(d_0 - z)}{\left[a^2 + (d_0 - z)^2\right]^4\left[c_2 + c_1\dfrac{B_0\,a^3}{\left[a^2 + (d_0 - z)^2\right]^{3/2}}\right]}\widehat{\mathbf{z}}, \tag{4}$$

where $\Delta\chi_p$ is the difference in magnetic susceptibility between the PMP and the surrounding medium (i.e. fluid solution), μ_0 is the magnetic permeability of free space and $\mathbf{B_m}$ is the magnetic flux-density of the permanent magnet, and the constants c_1 and c_2 are empirically determined using a best fit for the constants in the reciprocal relationship determined by Grob et al. (2018) between susceptibility of a PMP with magnetic field strength $\mathbf{B}$, see Fig. 4.a.ii and Supplementary Material Section S.2.5 for details. The force is shown in Fig. 4.a.iii as a function of distance from the face of the magnet using both the experimentally measured $\mathbf{B}$-field and that obtained from (3).

5.3. Movement of PMPs in fluid under magnetic field

We suppose that a cluster of n PMPs and bacteria, formed by agglutination, can be represented by a buoyant sphere of volume V, radius R_n. We can use the theory of Stokes flow to calculate the forces acting on the entire cluster when in the testing chamber and under the effect of a magnetic field (see Fig. 4.a.i):

$$\rho_p V\ddot{z} + 6\pi\mu R_n\dot{z} + \Delta\rho Vg = F_c^m, \tag{5}$$

Here, drag force, calculated using Stokes' Law $F_d = 6\pi\mu R_n\dot{z}$ on a sphere of radius R_n moving through a fluid with a coefficient of dynamic viscosity μ at velocity $\dot{z}$ (Stokes (2009)) and F_c^m is the vertical component of the magnetic force on the cluster. The density of a PMP is denoted ρ_p, it's relative density with that of the surrounding fluid is $\Delta\rho$ and g is gravitational field strength on earth.

The magnetic force experienced by a cluster of n PMPs is dependant on the volume of susceptible material (PMPs) present in the cluster. Thus $F_c^m = nF_p^m$, where n being the number of PMPs in the cluster and F_p^m is the z-component of the magnetic force on each PMP, given by (4). Here we are assuming that the magnetic flux density is the same at all points across the cluster (i.e. that the cluster is small in comparison to the flux density spatial variation). We assume the total volume of the cluster is $V = nV_p$ where V_p is the volume of a single PMP and has total radius $R_n = r_p n^{\frac{1}{3}}$ where r_p is the radius of a single PMP. Substituting these terms into equation (5) leads, after division by n, to an equation of motion of the form,

$$\rho_p V_p\ddot{z} + \frac{6\pi\mu r_p}{n^{\frac{2}{3}}}\dot{z} + \Delta\rho V_p g = F_p^m. \tag{6}$$

Note that equation (6) cannot be solved in closed form, but several important scaling observations can be made from it. First, a simple scaling analysis shows that the inertial term (first term on the right-hand side) is much smaller than the Stokes drag term (see 1 in Supplementary Material Section S.3 for a list of parameter values). Hence the dynamics is damping dominated and each cluster will quickly reach a terminal velocity within the chamber. Furthermore, note that only the Stokes drag is dependent on the number of PMPs, n. In particular, as the concentration of target bacteria increases, so the cluster size n increases, the drag force decreases, and thus the terminal velocity must increase, leading to more rapid motion.

5.4. Inductive coil response

In order to characterise the degree of agglutination from the assay, a model for the inductive response of the magnetometer was developed. An expression for the change in inductance, ΔL, of a axially-symmetric

planar coil to the presence of a single point-like paramagnetic particle (PMP) at some position (r, z) above the coil, was derived by Gal-Katziri and Hajimiri (2019), and can be approximated for a PMP in a solution with no magnetic susceptibility as,

$$\Delta L \approx \frac{V_p\chi_{AC}}{\mu_0 I}\mathbf{B_s}(r, z)^2, \tag{7}$$

where μ_0 is the magnetic permeability of free space, I is the current exciting the coil, while V_p is the PMP volume and χ_{AC} is the magnetic susceptibility of the PMP in the coils AC magnetic field (calculated via the same process as χ_p, see Supplementary Material, Section S.2.5) of the PMP respectively. This expression assumes that the presence of a PMP does not perturb the magnetic flux density above the coil.

The magnetic flux density, $\mathbf{B_s}(r, z)$, generated by the coil can be calculated via linear summation of the field generated by each of the N coil turns carrying current I corresponding to a PMP at a point (r_{pmp}, z_{pmp}). See the Supplementary Material, Section S.3.1 for details.

5.5. Simulation protocol

All simulations are carried out in Matlab, using the ordinary differential equation solver ode45. First, for each dose (ratio R of bacteria to PMP) the Becker-Döring equations are solved, using $N = 70$ until the concentrations of each size n reaches a steady state distribution, like the one shown in Fig. 4.c. This ensemble of values of n is fed into the Stokes drag term in equation (6) and an ensemble of trajectories computed using numerical integration to produce a description of motion of all the clusters for dose level. The initial displacement of each cluster is set at a fixed distance Δz from the top magnet. The corresponding trajectories $z_n(t)$ for different n are shown in Fig. 5.c. From these family of positions $z_n(t)$, we then use Eqn (7) to obtain the predicted inductive response $\Delta L_i(t)$ of the magnetometer for each cluster size i, which is then summed for all cluster sizes in a dose response distribution (see Fig. 4.c) to give the complete dose response curve ΔL.

5.6. Simulation results — the predicted heidelberger curve

The simulated results are shown in Fig. 5. For experimental measurements, the ideal metric of the transient response is the voltage peak, ΔV, and the area under the curve, A. However, for simulations, we assume an instantaneous magnetic pull and fixed number of PMPs, do not model an temporally increasing magnetic field on the clusters, or the introduction of the magnet on the magnetometer inductance, and so do not generate a similar voltage peak. Instead we measure the half-life Δt of the decay to final position, as explained in Fig. 5.d, which is directly proportional to A measured experimentally.

The simulated response curve in Fig. 5.e clearly shows a characteristic Heidelberger curve as in the experiments (Fig. 3.c-d). Moreover it is extremely encouraging that the minimum of the simulated curve is at a $R = 1$, which corresponds to a 1:1 ratio of dose of PMPs to bacteria. This shows that the there is a peak in the agglutination mechanism at this dose, which causes clusters to experience the greatest magnetophoretic force. Beyond this dose level we see the characteristic hook effect of the Heidelberger curve.

While there is excellent agreement on the shape of the curve, we note the discrepancy in values between the precise value of Δt in the theory compared with the experiment. This is likely due to a number of factors in the model, including; no gradual temporal increase in magnetic pull field, an artificial limit imposed on the size of clusters N, as well as the absence of cooperative magnetophoresis effects, which would further increase cluster sizes. Simulating larger cluster sizes is likely to lead, to larger magnetic forces compared with drag and hence lead to shorter decay times in simulations.

The results from this simulation also demonstrate the relationship between magnetic field strength and inductive response. Due to
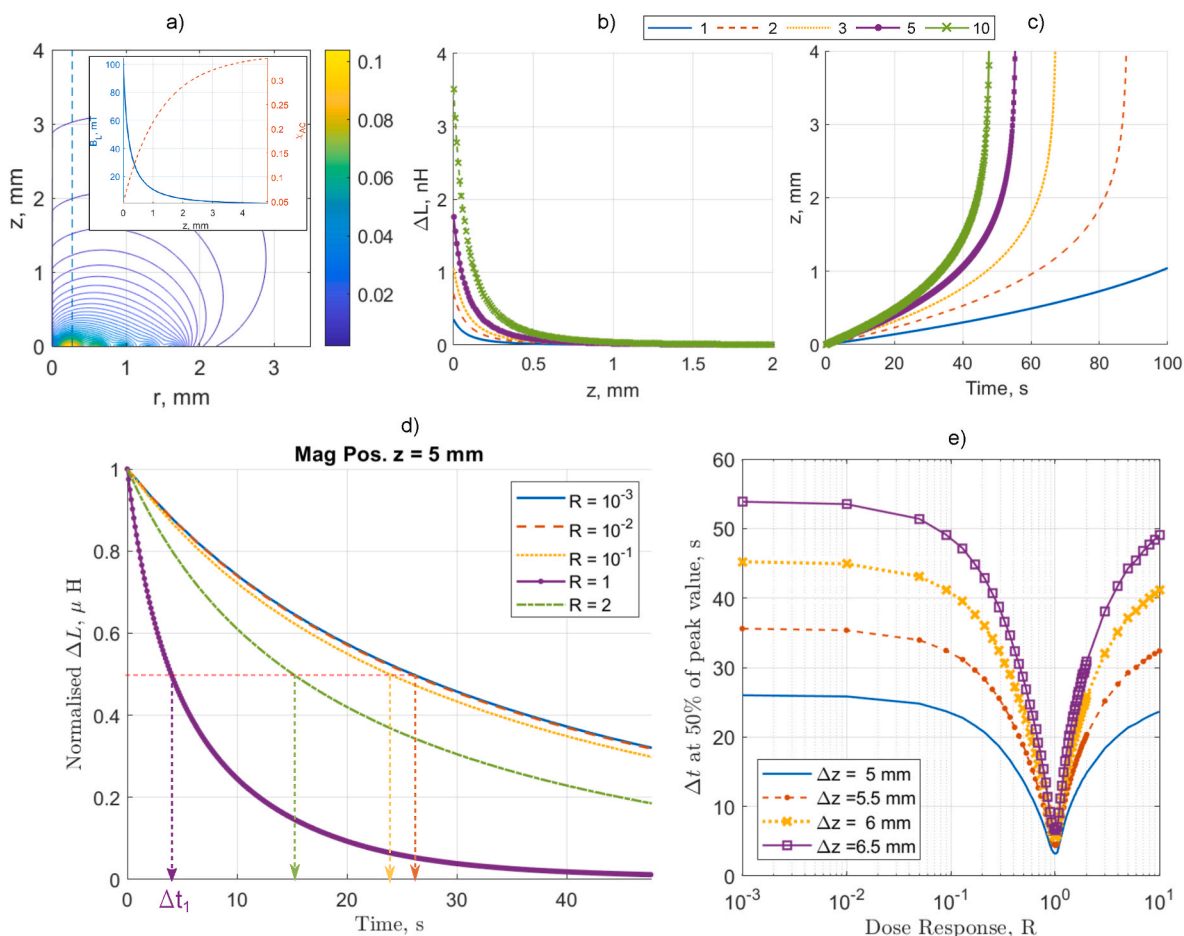
Fig. 5. Simulated inductive response to PMP clusters showing: a) The simulated peak magnetic flux density, *B*, above the inductive magnetometer with a 1D trial 'path' (dashed line) of PMP motion through the chamber during the magneto-assay, with the embedded figure showing *B* and the predicted magnetic susceptibility, χ_{AC}, as a function of distance along the path of a PMP. b) Shows the predicted change in magnetometer inductance ΔL for different PMP cluster sizes (number of PMPs in cluster), as a function of position. c) Shows the predicted trajectories of PMP cluster sizes in the magnetic field of a top magnet. d) Shows the predicted magnetometer time response for different PMP-bacteria dose response (*R* also called β), and e) shows the Δt metric as a function of *R* for different magnet positions above the bottom of the chamber.

instantaneous nature of the model and the asymptotic trend, peak amplitude cannot be determined. Instead, the time to half-maximum, Δt, is used as a comparable metric to the area-under-the-curve, *A*, used for experimental data. An important observation to make here is that the minimum Δt for a dose response $R = 1$ remains largely unchanged for all modelled positions of the magnet, thereby causing the dynamic measurement range to increase with larger magnetic distances. This suggests that magnet position could be a significant design consideration in order to optimise the sensitivity of the agglutination assay.

6. Conclusion

This paper introduces a physics-based end-to-end model for simulating biosensor assay measuring the concentration of target biomolecules via the combined effects of immuno-agglutination of paramagnetic particles, induced motion under dynamic magnetic fields and indirect position measurement of particles using an inductive magnetometer. Through the development of a novel Becker-Döring-like formalism for agglutination, the model accurately predicts the trends observed in the dose response (Heidelberger curve) of the biosensor. We believe that this will be of significant use in future studies for bioassay design.

While much work remains to enhance the model, as well as characterise and calibrate a particular commercial sensor, we believe our work provides a significant step towards demonstrating the feasibility of

bioassay sensor design, with profound implications for future point-of-care diagnostics.

CRediT authorship contribution statement

Robert Hughes: Electromagnetic and magnetodynamic modelling; experimental data analysis; co-wrote first draft. **Aaron Fishman:** Fluid mechanics modelling. **Kathryn Lamb-Riddell:** Carried out experimental measurements. **Alan Champneys:** Conceived agglutination model; co-wrote first draft. **Janice Kiely:** Sensor design. **Richard Luxton:** Design of biochemical assay.

Declaration of competing interest

The authors declare that they have no known competing financial interests or personal relationships that could have appeared to influence the work reported in this paper.

Data availability

Data are available at the University of Bristol data repository, data. bris, at https://doi.org/10.5523/bris.3jwcbeuxu42vv2d6y44ncg3soz.

Acknowledgements

Appendix A. Supplementary data

Supplementary data to this article can be found online at https://doi.org/10.1016/j.bios.2022.114745.

References

Ahmadivand, A., Gerislioglu, B., Manickam, P., Kaushik, A., Bhansali, S., Nair, M., Pala, N., 2017. Rapid detection of infectious envelope proteins by magnetoplasmonic toroidal metasensors. ACS Sens. 2, 1359–1368.

Ball, J., Carr, J., Penrose, O., 1986. The Becker-Döring cluster equations: basic properties and asymptotic behaviour of solutions. Commun. Math. Phys. 104, 657–692.

Barnett, J., Wraith, P., 2014. An inexpensive, fast and sensitive quantitative lateral flow magneto-immunoassay for total prostate specific antigen. Biosensors 4, 204–220.

Bean, D., Krahe, D., Wareham, D., 2008. Antimicrobial resistance in community and nosocomial Escherichia coli urinary tract isolates. Ann. Clin. Microbiol. Antimicrob. 7 https://doi.org/10.1186/1476-0711-7-13. London 2005-2006.

Becker, R., Döring, W., 1935. Kinetische behandlung der Keimbildung in übersättigten dämpfen. Ann. Phys. https://doi.org/10.1002/andp.19354160806.

Delaney, S., Suh-Lailam, B., 2018. Microfluidics: the future of testing? Clin. Chem. 64, 417, 417.

Faraudo, J., Andreu, J., Calero, C., Camacho, J., 2016. Predicting the self-assembly of superparamagnetic colloids under magnetic fields. Adv. Funct. Mater. 26, 3837–3858.

Foudeh, A., Didar, T., Veres, T., Tabrizian, M., 2012. Microfluidic designs and techniques using lab-on-a-chip devices for pathogen detection for point-of-care diagnostics. Lab Chip 12, 3249–3266.

Gal-Katziri, M., Hajimiri, A., 2019. Analysis and design of coupled inductive bridges for magnetic sensing applications. IEEE J. Solid State Circ. 54, 1883–1894.

Gopal, J., Abdelhamid, H., Huaa, P.Y., Wu, H.F., 2013. Chitosan nanomagnets for effective extraction and sensitive mass spectrometric detection of pathogenic bacterial endotoxin from human urine. J. Mater. Chem. B 1, 2463–2475.

Griffiths, D., 2008. Introduction to Electrodynamics, third ed. Pearson Benjamin Cummings.

Grob, D., Wise, N., Oduwole, O., Sheard, S., 2018. Magnetic susceptibility characterisation of superparamagnetic microspheres. J. Magn. Magn Mater. 452, 134–140.

He, P., Katis, I., Kumar, A., Bryant, C., Keevil, C., Somani, B., Mahobia, N., Eason, R., Sones, C., 2020. Laser-patterned paper-based sensors for rapid point-of-care detection and antibiotic-resistance testing of bacterial infections. Biosens. Bioelectron. 152.

Heidelberger, M., 1939. Chemical aspects of the precipitin and agglutinin reactions. Chem. Rev. 24, 323–343.

Heidelberger, M., Kendall, F., 1934. Quantitative studies on the precipitin reaction: the role of multiple reactive groups in antigen-antibody union as illustrated by an instance of cross-precipitation. J. Exp. Med. 59, 519–528.

Hönes, J., Müller, P., Surridge, N., 2008. The technology behind glucose meters. Test strips. https://doi.org/10.1089/dia.2008.0005.

Hu, G., Gao, Y., Li, D., 2007. Modeling micropatterned antigen-antibody binding kinetics in a microfluidic chip. Biosens. Bioelectron. 14, 1403–1409.

Hughes, R., Dixon, S., 2018. Analysis of electrical resonance distortion for inductive sensing applications. IEEE Sensor. J. 14, 5818–5825.

Islam, N., Saye, S., 2012. MEMS microfluidics for lab-on-a-chip applications. Microelectromechanical Systems and Devices.

Jang, J., Hur, H.G., Sadowsky, M., Byappanahalli, M., Yan, T., Ishii, S., 2017. Environmental Escherichia coli: ecology and public health implications—a review. J. Appl. Microbiol. 123, 570–581.

Kaper, J., Nataro, J., Mobley, H., 2004. Pathogenic Escherichia coli. Nat. Rev. Microbiol. 2, 123–140.

Kiely, J., Luxton, R., 2022. Health Tech Hub — Helping Tech Happen for Healthy Futures. URL: www.healthtechhub.co.uk. (Accessed 10 August 2022) https://www.healthtechhub.co.uk/.

Luppa, P., Müller, C., Schlichtiger, A., Schlebusch, H., 2011. Point-of-care Testing (POCT): Current Techniques and Future Perspectives.

Manz, A., Neuzil, P., O'Connor, J., Simone, G., 2020. Microfluidics and Lab-On-A-Chip. Royal Society of Chemistry, London.

McFarland, N., Bundle, N., Jenkins, C., Godbole, G., Mikhail, A., Dallman, T., O'Connor, C., McCarthy, N., O'Connell, E., Treacy, , et al.J, 2017. Recurrent seasonal outbreak of an emerging serotype of Shiga toxin-producing Escherichia coli (STEC O55: H7 Stx2a) in the south west of England. Euro Surveill. 22, 30610. July 2014 to September 2015.

Naseri, M., Ziora, Z., Simon, G., Batchelor, W., 2021. Assured — compliant point-of-care diagnostics for the detection of human viral infections. Rev. Med. Virol., e2263

O'Neill, J., 2014. Antimicrobial Resistance: tackling a crisis for the health and wealth of nations. The Review on Antimicrobial Resistance. Technical Report.

Pai, A., Khachaturian, A., Chapman, S., Hu, A., Wang, H., Hajimiri, A., 2014. A handheld magnetic sensing platform for antigen and nucleic acid detection. Analyst 139, 1403–1411. https://doi.org/10.1039/C3AN01947K.

Qu, J., Zhang, Y., Chenier, M., Xu, C., Chen, L., Wan, Y., 2021. A transit time-resolved microflow cytometry-based agglutination immunoassay for on-site C-reactive protein detection. Micromachines 12, 109.

Roberts, L., Griffith, T., Champneys, A., Piano, M., Kiely, J., Luxton, R., 2017. Mathematical modelling of a magnetic immunoassay. IMA J. Appl. Math. 82, 1253–1282.

Sachdeva, S., Davis, R., Saha, A., 2021. Microfluidic point-of-care testing: commercial landscape and future directions. Front. Bioeng. Biotechnol. 8.

Sharif, E., Kiely, J., Luxton, R., 2013. Novel immunoassay technique for rapid measurement of intracellular proteins using paramagnetic particles. J. Immunol. Methods 388, 78–85. https://doi.org/10.1016/j.jim.2012.11.015.

Shevkoplyas, S., Siegel, A., Westervelt, R., Prentiss, M.G., Whitesides, G., 2007. The force acting on a superparamagnetic bead due to an applied magnetic field. Lab Chip 7, 1294–1302.

Sista, R., Hua, Z., Thwar, P., Sudarsan, A., Srinivasan, V., Eckhardt, A., Pollack, M., Pamula, V., 2008. Development of a digital microfluidic platform for point of care testing. Lab Chip 8, 2091–2104.

Sleigh Muñoz, V., 2020. Mathematical modelling of a micro-fluidic sensor for biological pathogens. Masters Thesis, Engineering Mathematics. University of Bristol.

Stavitsky, A., 1998. Agglutination. In: Encyclopedia of Immunology.

Stenutz, R., Weintraub, A., Widmalm, G., 2006. The structures of Escherichia coli O-polysaccharide antigens. FEMS (Fed. Eur. Microbiol. Soc.) Microbiol. Rev. 30, 382–403.

Stokes, G., 2009. On the effect of the internal friction of fluids on the motion of pendulums. In: Mathematical and Physical Papers. Cambridge University Press, Cambridge, pp. 1–10. https://doi.org/10.1017/CBO9780511702266.002. URL: https://www.cambridge.org/core/product/identifier/CBO9780511702266A006/type/book_part.

Tepeli, Y., Ülkü, A., 2018. Electrochemical biosensors for influenza virus a detection: the potential of adaptation of these devices to POC systems. Sens. Actuators, B 254, 377–384.

Tsouris, C., Scott, T., 1995. Flocculation of paramagnetic particles in a magnetic field. J. Colloid Interface Sci. 171, 319–330. https://doi.org/10.1006/jcis.1995.1186.

Wang, C., Liu, M., Wang, Z., Li, S., Deng, Y., He, N., 2021. Point-of-care diagnostics for infectious diseases: from methods to devices. Nano Today 37, 101092.

Wang, X., Li, F., Guo, Y., 2020. Recent trends in nanomaterial-based biosensors for point-of-care testing. Front. Chem. 8, 924.

Wattis, J., King, J., 1998. Asymptotic solutions of the Becker-Döring equations. J. Phys. Math. Gen. 31, 7169–7189.

Wu, L., Ye, M., Qin, X., Liu, Y., Lv, Z., Zheng, R., 2020. Diagnostic value of quantitative MP-IgG for Mycoplasma pneumoniae pneumonia in adults. Clinica Chimica Acta; International Journal of Clinical Chemistry 503, 76–83.

Wua, D., Voldman, J., 2020. An integrated model for bead-based immunoassays. Biosens. Bioelectron. 154, 112070.